Arch. Mech., 32, 3, pp. 369-388, Warszawa 1980

Lattice rotations and localized shearing in single crystals

Y. W. CHANG and R. J. ASARO (PROVIDENCE)

LOCALIZED shearing in ductile single crystals undergoing multiple slip is studied using the simple model, introduced by ASARO [1], for a crystal deformed in tension with symmetric double slip. Special attention is paid to the model predictions concerning the kinematics of localized shearing, in particular the predictions of local lattice rotations, and these, as well as the predictions for a critical ratio of slip plane strain-hardening rate to tensile stress, are compared to experiment. The effects of "local lattice rotations" on the formation and initial development of macroscopic shear bands in Al-3 wt percent Cu single crystals were studied experimentally for crystals deformed in simple tension and compression. X-ray diffraction, and Berg-Barrett topography, revealed that the lattice within the shear bands was finitely rotated from that of the surrounding crystal parts, and that this rotation was always such as to induce "geometrical softening" within the bands. The character of the observed local rotations is in essential accord with the predictions of our recent continuum analyses of localized plastic deformation in single crystals whereas the mechanistics of the rotation process is most simply explained by the dislocation theory through the formation of Lomer-Cottrell locks.

Rozpatruje się zlokalizowane ścinanie w monokryształach poddanych wielokrotnym poślizgom posługując się prostym modelem wprowadzonym przez ASARO [1] dla kryształu rozciąganego z podwójnym symetrycznym poślizgiem. Szczególną uwagę zwraca się na przewidzianą tym modelem kinematykę zlokalizowanego ścinania, a w szczególności na lokalne obroty sieci; wyniki te, a również przewidywania dotyczące krytycznej wartości stosunku prędkości wzmocnienia na płaszczyźnie poślizgu do naprężeń rozciągających, porównano z doświadczeniami. Wpływ «lokalnych obrotów sieci» na tworzenie się i rozwój makroskopowych pasm ścinania w monokryształach Al-3% Cu zbadano eksperymentalnie na kryształach poddanych prostemu rozciąganiu i ściskaniu. Dyfrakcja rentgenowska i topografia Berga-Barreta wykazują, że sieć w obrębie pasm ścinania podlega skończonemu obrotowi względem kryształów otaczających, a obrót ten jest zawsze tego rodzaju, że wprowadza do pasm «geometryczne zmiękczenie». Charakter zaobserwowanych obrotów lokalnych zgadza się w zasadzie z naszymi kontynualnymi analizami dotyczącymi zlokalizowanych odkształceń plastycznych w monokryształach, podczas gdy mechanizm procesu obrotów wytłumaczyć można najłatwiej za pomocą teorii dyslokacji i tworzeniem się zamków Lomera-Cottrella.

Рассматривается локализированный сдвиг в монокристаллах, подвергнутых многократным скольжениям, послуживаясь простой моделью, введенной ACAPO [1] для кристалла растягиваемого с двойным симметричным скольжением. Особенное внимание обращается на предсказываемую этой моделью кинематику локализированного сдвига, в частности на локальные вращения решетки; эти результаты, а тоже предсказывания, касающиеся критического значения отношения скорости упрочнения на плоскости скольжения к растягивающим напряжениям, сравнены с экспериментами. Влияние „локальных вращений решетки" на образование и развитие макроскопических полос сдвига в монокристаллах Al — 3% Cu экспериментально исследовано на кристаллах, подвергнутых простому растяжению и сжатию. Рентгеновская дифракция и топография Берга-Баррета показывают, что решетка в области полос сдвига подлежит конечному вращению по отношению к окружающим кристаллам, а это вращение всегда этого рода, что вводит в полосы „геометрическое смягчение". Характер наблюдаемых локальных вращений совпадает в принципе с нашими континуальными анализами, касающимися локализированных пластических деформаций в монокристаллах, в то время как механизм процесса вращений можно объяснить самым простым образом при помощи теории дислокаций и образованием замков Ломера-Коттрелла.

Introduction

WHEN ductile single crystals of uniform dimensions and material properties are plastically deformed, the initial, typically uniform macroscopic pattern of flow invariably becomes localized as necks and eventually into bands of intensely localized shear. Of these two non-uniform modes, localized shearing is of particular interest, not only because it appears to be a natural inherent occurrence in apparently homogeneous, perfect, strain-hardening solids, but also since it is very often a direct precursor to ductile failure. Recent theoretical studies of the phenomena [1, 2] have shown, in accordance with experiment [3], that the formation of shear bands is indeed possible even in imperfection free, positively strain-hardening crystals and thus in materials which are neither softening [4] or undergoing fracture. Asaro's recent model, described in Sects. 2 and 3, for crystals deforming by double slip is of particular interest here in that the kinematics of localized shearing he analyzed have some important crystallographic implications regarding lattice rotations within the shear bands leading to local "geometrical softening" which we have recently uncovered experimentally in Al—Cu crystals. The present paper describes some of the more important results of these experiments, especially those on "local lattice rotations" within shear bands.

Although the idealized geometry considered by ASARO [1] differs slightly from that of fcc Al—Cu crystals, its kinematical description of deformation is indeed very similar to that of the actual crystal. Furthermore, the model's predictions for localized shearing are in excellent agreement with our experimental findings. The model is discussed in some detail in Sects. 2 and 3. In Sect. 3 a direct correspondence is made between the crystal model and the orthotropic, plane strain, incompressible solid studied by HILL and HUTCHINSON [5]. Their bifurcation solutions, leading to non-uniform deformation modes, are discussed by MILES [6] elsewhere.

Section 2 provides a brief description of the constitutive laws. Section 4 describes some experimental results, and in Sect. 5 a dislocation model which helps explain the mechanistics of the observed and predicted lattice rotations is presented.

2. Constitutive laws for single crystals deforming by crystallographic slip

Constitutive laws for single crystals are formulated in accord with the kinematic scheme presented by ASARO and RICE [2], which was in fact based upon the analysis of HILL and RICE [7]. The generalization to multiple slip was made by ASARO [1] and applied to the crystal model shown in Fig. 1; the reader can refer to those papers for detailed discussions — a brief description follows below.

The total deformation and rotation of the crystal is taken as the superposition of a set of simple plastic shears on the currently active slip systems, with rates $\dot{\gamma}^{(\alpha)}$, and a general lattice deformation and rotation denoted by $\mathbf{D}^*$ and $\mathbf{\Omega}^*$. The plastic contribution to the rates of material deformation and rotation are then given by

$$\sum_{\alpha} \mathbf{p}^{(\alpha)}\dot{\gamma}^{(\alpha)} \quad \text{and} \quad \sum_{\alpha} \boldsymbol{\omega}^{(\alpha)}\dot{\gamma}^{(\alpha)},$$

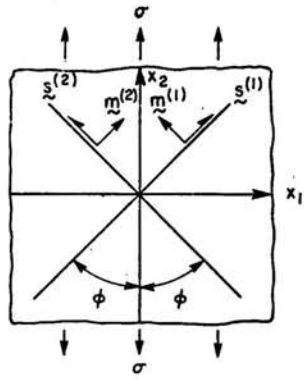

FIG. 1. Plane orthotropic crystal model for a single crystal deforming by symmetric double slip, in tension or compression. The model assumes that the slip plane normals, **m**, slip directions, **s**, and loading axis, **t**, are all in the drawing's plane. ϕ is the angle either slip plane makes with the **t**. $\phi \approx 35$ degrees is used to model a fcc crystal aligned for primary-conjugate slip, whereas $\phi \approx 55$ degrees can be used to model certain bcc crystals with $\mathbf{t} \| \langle 111 \rangle$ as described for example by REID *et al.* [9].

respectively, where

$$\mathbf{p}^{(\alpha)} = \frac{1}{2}(\mathbf{s}^{(\alpha)}\mathbf{m}^{(\alpha)} + \mathbf{m}^{(\alpha)}\mathbf{s}^{(\alpha)}) \tag{2.1}_1$$

and

$$\boldsymbol{\omega}^{(\alpha)} = \frac{1}{2}(\mathbf{s}^{(\alpha)}\mathbf{m}^{(\alpha)} - \mathbf{m}^{(\alpha)}\mathbf{s}^{(\alpha)}). \tag{2.1}_2$$

The unit vectors $\mathbf{s}^{(\alpha)}$ and $\mathbf{m}^{(\alpha)}$ are the current slip direction and slip plane normal for the slip system α, and the sums are taken over "active" slip systems only. Addition of the plastic and lattice contributions yields, in component form,

$$D_{ij} = \frac{1}{2}(\partial v_i/\partial x_j + \partial v_j/x_i) = D^*_{ij} + \sum_\alpha p^{(\alpha)}_{ij}\dot{\gamma}^{(\alpha)} \tag{2.2}_1$$

and

$$\Omega_{ij} = \frac{1}{2}(\partial v_i/\partial x_j - \partial v_j/\partial x_i) = \Omega^*_{ij} + \sum_\alpha \omega^{(\alpha)}_{ij}\dot{\gamma}^{(\alpha)}; \tag{2.2}_2$$

v is the vector of particle velocity. An important point to be noticed concerning this kinematical description of crystalline deformation is that the rate of the lattice rotation, $\boldsymbol{\Omega}^*$, is composed of both rigid body rotations — these can be arbitrarily large — and spins of the lattice (and its associated vectors $\mathbf{s}^{(\alpha)}$ and $\mathbf{m}^{(\alpha)}$) due to elastic distortion — these are usually very small, on the order of stress, or stress rates divided by elastic moduli.

We take the lattice deformation to be elastic and **L** the tensor of elastic moduli phrased relative to lattice directions. Then

$$\overset{\nabla}{\boldsymbol{\sigma}}{}^* + \boldsymbol{\sigma}\,\mathrm{tr}\,(\boldsymbol{D}^*) = \mathbf{L}:\mathbf{D}^*, \tag{2.3}$$

where

$$\overset{\nabla}{\boldsymbol{\sigma}}{}^* = \dot{\boldsymbol{\sigma}} - \boldsymbol{\Omega}^* \cdot \boldsymbol{\sigma} + \boldsymbol{\sigma} \cdot \boldsymbol{\Omega}^*. \tag{2.4}$$

$\overset{\nabla}{\boldsymbol{\sigma}}{}^{*}$ is the Jaumann co-rotational stress rate of true stress, $\boldsymbol{\sigma}$, and as implied by Eq. (2.4), its components are formed on axes that spin with the *lattice*. To study material deformation on the other hand, we require a stress rate whose components are formed on axes that spin with the material as given by

$$\overset{\nabla}{\boldsymbol{\sigma}} = \dot{\boldsymbol{\sigma}} - \boldsymbol{\Omega}\cdot\boldsymbol{\sigma} + \boldsymbol{\sigma}\cdot\boldsymbol{\Omega}. \tag{2.5}$$

The two rates in Eqs. (2.4) and (2.5) are related by

$$\overset{\nabla}{\boldsymbol{\sigma}} - \overset{\nabla}{\boldsymbol{\sigma}}{}^{*} = \sum_{\alpha} (\boldsymbol{\sigma}\cdot\boldsymbol{\omega}^{(\alpha)} - \boldsymbol{\omega}^{(\alpha)}\cdot\boldsymbol{\sigma})\dot{\gamma}^{(\alpha)}. \tag{2.6}$$

Now if $\mathbf{D}^{*}$ in and $\boldsymbol{\Omega}^{*}$ Eqs. (2.3) and (2.4) are expressed in terms of $\mathbf{D}$ and $\boldsymbol{\Omega}$, then Eq. (2.3) becomes, with Eq. (2.6),

$$\overset{\nabla}{\boldsymbol{\sigma}} + \boldsymbol{\sigma}\,\mathrm{tr}(\mathbf{D}) = \mathbf{L} : \Big\{\mathbf{D} - \sum_{\alpha} \hat{\mathbf{p}}^{(\alpha)}\dot{\gamma}^{(\alpha)}\Big\}, \tag{2.7}$$

where

$$\hat{\mathbf{p}}^{(\alpha)} = \mathbf{p}^{(\alpha)} + \mathbf{L}^{-1} : (\boldsymbol{\omega}^{(\alpha)}\cdot\boldsymbol{\sigma} - \boldsymbol{\sigma}\cdot\boldsymbol{\omega}^{(\alpha)}). \tag{2.7'}$$

A relation between $\dot{\gamma}^{(\alpha)}$ and the stress rate is now required.

We assume that yielding on each active slip system begins and continues when $\tau_{ms}^{(\alpha)} = (\mathbf{m}^{(\alpha)}\cdot\boldsymbol{\sigma}\cdot\mathbf{s}^{(\alpha)})$ reaches and maintains a critical value (which depends on strain). Then if the α system is to remain active, we must have

$$d/dt(\mathbf{m}^{(\alpha)}\cdot\boldsymbol{\sigma}\cdot\mathbf{s}^{(\alpha)}) = \sum_{\alpha} h\alpha\beta\dot{\gamma}^{(\beta)}. \tag{2.8}$$

$h\alpha\beta$ are the elements of a slip plane hardening matrix, the off-diagonal elements of which represent "latent", or coupled, hardening. ASARO and RICE [2] have discussed various possible ways of interpreting the left-hand-side of Eq. (2.7); for the present we will assume, following ASARO [1], that $\mathbf{m}^{(\alpha)}$ and $\mathbf{s}^{(\alpha)}$ simply rotate rigidly at the lattice spin rate $\boldsymbol{\Omega}^{*}$. Then

$$d/dt(\mathbf{m}^{(\alpha)}\cdot\boldsymbol{\sigma}\cdot\mathbf{s}^{(\alpha)}) = \mathbf{m}^{(\alpha)}\cdot\overset{\nabla}{\boldsymbol{\sigma}}{}^{*}\cdot\mathbf{s}^{(\alpha)} = \mathbf{p}^{(\alpha)} : \overset{\nabla}{\boldsymbol{\sigma}}{}^{*}. \tag{2.8'}$$

Evaluating $\overset{\nabla}{\boldsymbol{\sigma}}{}^{*}$, using Eq. (2.3) and replacing $\mathbf{D}^{*}$ and $\boldsymbol{\Omega}^{*}$ with $\mathbf{D}$ and $\boldsymbol{\Omega}$, Eq. (2.8) becomes

$$\mathbf{L} : \Big\{\mathbf{D} - \sum_{\beta} \mathbf{p}^{(\beta)}\dot{\gamma}^{(\beta)}\Big\} : \mathbf{p} = \sum_{\beta} h\alpha\beta\dot{\gamma}^{(\beta)} \tag{2.9}$$

which, when inverted, yields

$$\dot{\gamma}^{(\beta)} = \sum_{\alpha} \{h\alpha\beta + \mathbf{p}^{(\alpha)} : \mathbf{L} : \mathbf{p}^{(\beta)}\}^{-1}\mathbf{p}^{(\alpha)} : \mathbf{L} : \mathbf{D}. \tag{2.10}$$

By combining Eq. (2.10) with Eq. (2.7) we obtain

$$\overset{\nabla}{\boldsymbol{\sigma}} + \boldsymbol{\sigma}\,\mathrm{tr}(\mathbf{D}) = \mathbf{L} : \mathbf{D} - \mathbf{L} : \sum_{\alpha,\beta}{}' \hat{\mathbf{p}}^{(\alpha)} N_{\alpha\beta}^{-1}\mathbf{p}^{(\beta)} : \mathbf{L} : \mathbf{D} \tag{2.11}$$

or its inverse,

$$\mathbf{D} = \mathbf{L}^{-1} : \{\overset{\nabla}{\boldsymbol{\sigma}} + \boldsymbol{\sigma}\,\mathrm{tr}(\mathbf{D})\} + \sum_{\alpha,\beta} \hat{\mathbf{p}}^{(\alpha)} N^{-1}_{\alpha\beta} (\mathbf{p}^{(\beta)} : \mathbf{L} : \mathbf{D}), \tag{2.12}$$

$\mathbf{N}^{-1}$ is the matrix whose elements appear in brackets in Eq. (2.10).

To reformulate Asaro's model, for the crystal geometry of Fig. 1, we first assume that the crystal's elasticity is isotropic and incompressible. Then tr $(\mathbf{D}) = 0$ and the first term in Eq. (2.12) is $(2G)^{-1}\overset{\nabla}{\boldsymbol{\sigma}}$, where G is the elastic shear modulus. Next, for this crystal assumed to be undergoing a nearly symmetric double mode of slip, we take $h\alpha\beta$ to have the elements $h_{11} = h_{22} = h$ and $h_{12} = h_{21} = h_1$ — now the summations over α and β range from 1 to 2. For the present case of simple tension along x_2, the only non-zero stress component is $\sigma_{22}(= \sigma)$. Also, for the geometry of Fig. 1,

$$\begin{aligned} s_1^{(1)} &= \sin\phi, & s_1^{(2)} &= -\sin\phi, \\ s_2^{(2)} &= \cos\phi, & s_2^{(2)} &= \cos\phi, \\ m_1^{(1)} &= -\cos\phi, & m_1^{(2)} &= \cos\phi, \\ m_2^{(1)} &= \sin\phi, & m_2^{(2)} &= \sin\phi. \end{aligned} \tag{2.13}$$

Using Eq. (2.13) and the above constitutive assumptions, Eq. (2.12) yields the following constitutive laws for what amounts to an orthotropic, incompressible, pressure insensitive material:

$$\begin{aligned} \overset{\nabla}{\sigma}_{22} - \overset{\nabla}{\sigma}_{11} &= \frac{2G(h+h_1)}{(h+h_1)+2G\sin^2 2\phi}\,(D_{22}-D_{11}), \\ \overset{\nabla}{\sigma}_{12} &= \frac{2G(h-h_1+\sigma\cos 2\phi)}{(h-h_1)+2G\cos^2 2\phi}\,D_{12}, \\ D_{11}+D_{22} &= 0. \end{aligned} \tag{2.14}$$

Before using the above relations to formulate the localization conditions we note two interesting features contained within them.

2.1. Yield vertexes

The term $2G\cos^2 2\phi$ in the denominator of Eq. (2.14_2) actually represents a vertex on the crystal's yield surface. The vertex softening implied is extremely pronounced in that the incremental effective "shear modulus" multiplying the shear deformation rate D_{12} in Eq. (2.14_2) rapidly decreases from the elastic value $2G$ when $\phi = \pi/4$, to values of the order of the slip plane strain-hardening rate, h, when $\phi \approx 35°$. This latter value for ϕ would represent a face-centered-cubic crystal, tested in tension so that the tensile axis rotates toward the [001]—[$\bar{1}$11] symmetry boundary. The origin of the vertex is simple to understand: if $\phi = \pi/4$, then simple shears on the slip systems cause no shear along the geometric axes, x_1 and x_2; the response is thus elastic with stiffness $2G$. If ϕ deviates from $\pi/4$, simple shears along the slip systems do contribute to D_{12} and the response is elastic-plastic and thus much softer. Although uniform extension of the crystal (at rate D_{22}) is described by Eq. (2.14_1) — the incremental slope of the σ_{22} versus extensional strain

curve is $\frac{4G(h+h_1)}{(h+h_1)+2G\sin 2\phi^2}$ — the localized shearing modes discussed shortly involve shearing along the geometric axis (at rate D_{12}). For this reason vertexes and vertex softening in shear can play an important role in destabilizing uniform extension.

2.2. Geometrical softening

Another important and novel feature of our crystalline constitutive laws in Eq. (2.14) is their description of "geometrical softening", through the term $\sigma\cos 2\phi$ in the numerator of Eq. (2.14_2), due to rotations of the crystal's lattice in the current stress field. This term arises by our accounting for the differences in $\overset{\nabla}{\boldsymbol{\sigma}}$ and $\overset{\nabla}{\boldsymbol{\sigma}}{}^*$ as in Eq. (2.6). As worked out by Asaro, this term in fact completely describes geometrical softening in a tension test for a crystal undergoing single slip. The importance of geometrical softening will become evident in examining the shear band solutions of the next section.

3. Localized shear bands

The structure of the incremental relations (2.14) is identical to that developed by BIOT [8] and more recently studied by HILL and HUTCHINSON [5] for orthotropic, pressure insensitive materials deforming in plane strain. A formal correspondence is made by identifying the moduli μ and μ^* (cf. HILL and HUTCHINSON [5] p. 240, Eq. 21) and rewriting Eq. (2.14);

$$\begin{aligned} \overset{\nabla}{\sigma}_{22}-\overset{\nabla}{\sigma}_{11} &= 2\mu^*(D_{22}-D_{11}), \\ \overset{\nabla}{\sigma}_{12} &= 2\mu D_{12}, \\ D_{11}+D_{22} &= 0. \end{aligned} \tag{3.1}$$

The comprehensive bifurcation analyses worked out by these authors should now still apply to our crystal model if special care is taken to allow for possible negative values for μ. Bifurcation solutions in plane strain tension for this material are also discussed by MILES [6]. Here we will limit our attention to localized shearing modes.

To proceed we introduce the nominal stress, t_{ij}. Its definition is that, beginning at time t, $\dot{t}_{ij}$ is the rate of change of the x_j component of load acting on a plane material element which *was* perpendicular to the x_i axis and *had* unit area. Since the only non-zero current true stress component is $\sigma_{22}\,(=\sigma)$, the components of $\dot{\mathbf{t}}$ are

$$\begin{aligned} \dot{t}_{11} &= \overset{\nabla}{\sigma}_{11}, \quad \dot{t}_{22} = \overset{\nabla}{\sigma}_{22}-\sigma\frac{\partial v_2}{\partial x_2}, \\ \dot{t}_{12} &= \overset{\nabla}{\sigma}_{12}-\sigma D_{12} = \dot{\sigma}_{12}-2\sigma\Omega_{12}, \\ \dot{t}_{21} &= \overset{\nabla}{\sigma}_{21}+\sigma\Omega_{12} = \dot{\sigma}_{21}. \end{aligned} \tag{3.2}$$

Continuing equilibrium requires that

$$\frac{\partial \dot{t}_{ij}}{\partial x_i} = 0. \tag{3.3}$$

We now seek solutions to Eq. (3.3), given the constitutive laws (2.14) or (3.1) and (3.2) corresponding to velocity fields of the form

$$v_i = g_i f(\mathbf{n} \cdot \mathbf{x}). \tag{3.4}$$

If $f'' \neq 0$ (with real $\mathbf{n}$), this corresponds to non-uniform shear across planes with unit normal $\mathbf{n}$, in directions $\mathbf{g}$; for the incompressible material behavior assumed, $\mathbf{g} \cdot \mathbf{n} = 0$.

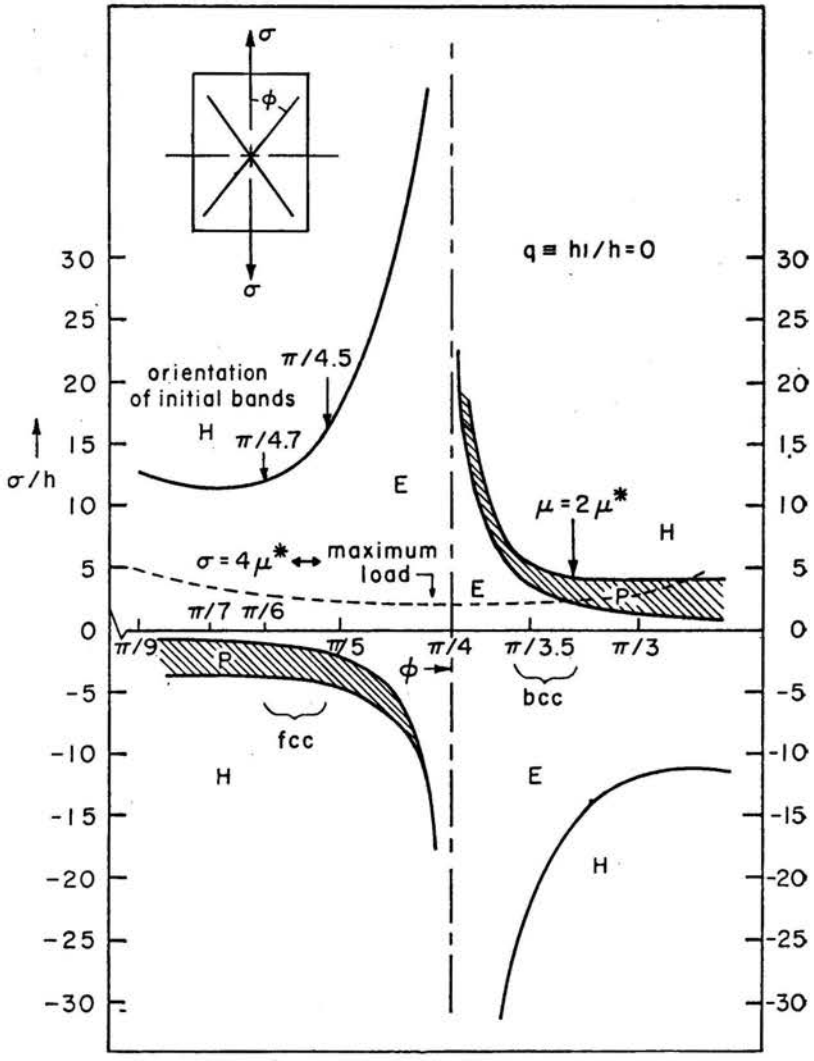

FIG. 2. Elliptic-hyperbolic-parabolic regimes for the crystal model shown in Fig. 1. For the cases where $\phi = 30$ and 35 degrees, the orientations of the first bands (i.e. θ) are indicated.

The conditions required for such solutions to satisfy continuing equilibrium (they are already compatible) are derived in a fashion identical to that discussed by HILL and HUTCHINSON [5] (cf. their equation A-10) — the result is the following consistency equation for $\mathbf{n}$:

$$\left(\mu-\frac{1}{2}\sigma\right)n_1^4+2(2\mu^*-\mu)n_1^2n_2^2+\left(\mu+\frac{1}{2}\sigma\right)n_2^4=0. \tag{3.5}$$

Shear bands may exist if *real* $\mathbf{n}$'s exist satisfying Eq. (3.5).

A general picture for shear bands emerges when we recognize that real $\mathbf{n}$'s imply either a parabolic or hyperbolic nature of Eq. (3.3) depending upon whether there are 2 or 4 real characteristics of Eq. (3.5), or in other words 1 or 2 real, positive values for $(n_2/n_1)^2$. Let the material be rigid plastic and $q \equiv h_1/h = 0$, for example. The results are then shown in Fig. 2 for a range of values for ϕ. Typically for low values of (σ/h) the equilibrium equations are elliptic and shear bands do not exist; as this ratio increases, with strain, either the elliptic-hyperbolic or elliptic-parabolic boundary is crossed; this depends upon whether ϕ is less or greater than $\pi/4$. Furthermore, whether shear bands appear before or after load-maxima are reached — $\sigma = 4\mu^*$ corresponds to a load maximum and now $4\mu^* = \dfrac{2(h+h_1)}{\sin^2 2\varphi}$ — also depends on ϕ or as discussed by HILL and HUTCHINSON [5] on whether $\mu/(2\mu^*)$ is less or greater than unity. The curve representing load maximum is also shown in the figure. Now, as discussed by ASARO [1] the present crystal model can be used to model fcc or some cases of bcc [9] crystals tested in tension. Appropriate choices for ϕ would be $\phi(\text{fcc}) \approx 30$–$35$ degrees whereas $\phi(\text{bcc}) \approx 50$–$55$ degrees. The model thus indicates that bcc crystals can be less stable than fcc crystals in that $(\sigma/h)_{\text{critical}}$ is lower.

Our experiments described in the next section were conducted on fcc, Al-3 wt percent Cu single crystals. When localized shearing (or necking) set in, the tensile axis generally had rotated to (or within a few degrees of) the [001]–[$\bar{1}$11] symmetry boundary. The deformation pattern was then one of nearly symmetric primary-conjugate slip and to model this we will take $\phi = 35$ degrees. Then, in Eq. (3.1) $\mu > 2\mu^* > 0$ and real $\mathbf{n}$'s exist when

$$(h/\sigma) \leqslant \frac{\cos 2\phi \pm \dfrac{\sin 4\phi}{\sqrt{2(1+q)}}}{2(q+\cos 4\phi)} \sin^2 2\phi; \qquad q \equiv h_1/h. \tag{3.6}$$

The equality sign yields the critical value and with $\phi = 35$ degrees

$$(h/\sigma)_{\text{critical}} = \begin{cases} 0.064 & q = 0, \\ 0.040 & q = 1, \\ 0.028 & q = 2. \end{cases} \tag{3.7}$$

Alternatively we may pose the following question: what are the conditions leading to a shear band inclined at angle θ to the x_2-axis, as depicted in Fig. 3? The band forms between two surfaces across which the deformation rates are discontinuous by the quan-

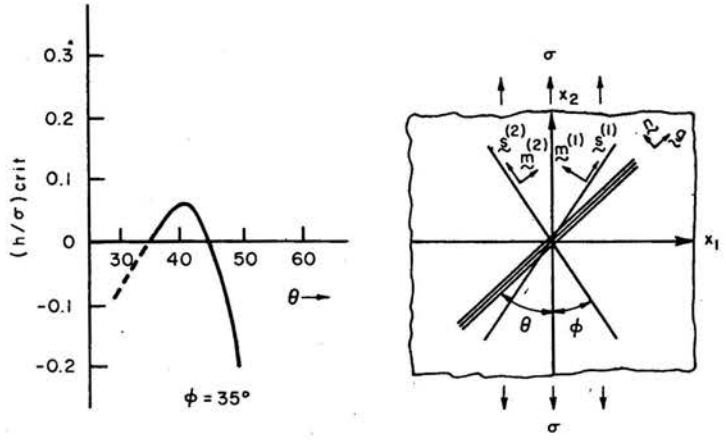

FIG. 3. Plot of the critical ratio of h, the slip plane hardening rate, to σ, the current tensile stress, for localized shearing in a band inclined by the angle θ to the tensile axis. The crystal model, shown on the right, is an idealized plane double slip with both slip plane normals, slip directions, and tensile axis in the drawing's plane.

tity $\lambda \mathbf{p}^{(3)}$; $\mathbf{p}^{(3)}$ is given by 1/2 $(\mathbf{gn}+\mathbf{ng})$ where λ is the magnitude of the jump in velocity and now both $\mathbf{g}$ and $\mathbf{n}$ are unit vectors. $\mathbf{g}$ and $\mathbf{n}$, for example, can have the same form as $\mathbf{s}^{(1)}$ and $\mathbf{m}^{(1)}$ in Eq. (2.13) with θ replacing ϕ. The equilibrium conditions are now applied directly — for the initially homogeneous crystal the condition is that the in-plane jump in stress rate across the band's surface vanish,

$$n_i[\dot{\sigma}_{ij}^{\text{inside}} - \dot{\sigma}_{ij}^{\text{outside}}] = 0. \tag{3.8}$$

By using the constitutive laws for the rigid plastic idealization, again as an example, Eq. (3.8) yields

$$(h/\sigma)_{\text{critical}} = \frac{\cos 2\theta - \cos^2 2\theta/\cos 2\phi}{(1-q)\cos^2 2\theta/\cos^2 2\phi + (1+q)\sin^2 2\theta/\sin^2 2\phi}. \tag{3.9}$$

As before, we take $q = 0$ and display some results for $\phi = 35$ degrees in Fig. 3. There are several important implications to be drawn from these results and which can be compared to our experiments on aluminum alloy crystals.

In the range $35 \leqslant \theta \leqslant 45$ degrees the critical (h/σ) ratio is *positive* so that with positive σ, localized shearing is predicted with positive h. Available latent hardening data suggests that q falls within the range $0 < q < 1$ and thus we expect, approximately, that $0.40 < (h/\sigma)_{\text{critical}} < 0.64$. Now since h generally decreases and σ increases, with strain near the points of localization the largest $(h/\sigma)_{\text{critical}}$ ratio, which occurs at $\theta = 40$ degrees, can be considered optimum. Thus the bands are predicted to be rotated from the slip planes by several degrees away from the tensile axis. We examine the kinematical implications further.

The *difference* in the velocity gradient across the band we recall has the form

$$\Delta\left(\frac{\partial \mathbf{v}}{\partial \mathbf{x}}\right) = \left(\frac{\partial \mathbf{v}}{\partial \mathbf{x}}\right)_{\text{band}} - \left(\frac{\partial \mathbf{v}}{\partial \mathbf{x}}\right)_{\text{matrix}} = \lambda \mathbf{gn} \tag{3.10}$$

with $(g_1, g_2) = (\sin\theta, \cos\theta)$ and $(n_1, n_2) = (-\cos\theta, \sin\theta)$. If we recognize that this jump involves essentially plastic deformations, we find, after setting $\Delta\mathbf{D} = \lambda/2(\mathbf{gn}+\mathbf{ng})$, that

$$\Delta(\dot{\gamma}^{(1)} - \dot{\gamma}^{(2)}) = \lambda\cos 2\theta/\cos 2\phi. \tag{3.11}$$

Similarly, from the jump in material spin rate $\Delta\mathbf{\Omega} = \lambda/2(\mathbf{gn}-\mathbf{ng})$, we find by forming both sides of Eq. (2.2_2) that

$$\Delta\Omega_{12} = \Delta\Omega^*_{12} + \lambda/2\cos 2\theta/\cos 2\phi = \lambda/2, \tag{3.12}_1$$

or

$$\Delta\Omega^*_{12} = \lambda/2[1 - \cos 2\theta/\cos 2\phi], \tag{3.12}_2$$

or

$$\Delta\Omega^*_{12} = \frac{\Delta D_{22}}{\sin 2\theta}[1 - \cos 2\theta/\cos 2\phi]. \tag{3.12}_3$$

Since elastic contributions to this difference in lattice spin rate are negligible (they are zero for the rigid plastic model), $\Delta\Omega^*_{12}$ is interpreted as a finite spin of the lattice in the band relative to that outside. Again, taking $\phi = 35$ and $\theta = 40$ degrees as examples, we find that $\Delta\Omega^*_{12} \approx 0.246\ \lambda$ (radians) $14.1\ \lambda$ (degrees). To gain some appreciation for the magnitude of rotation implied by this, let $\lambda dt = 0.1$ (dt is a time increment), i.e. let an approximately 10 percent excess shear strain increment develop in the band; then $\Delta\Omega^*_{12}\, dt \approx 1.41$ degrees. In other words, one-to-several degrees of rotation are implied by a 10-to-30 percent strain increment. It is important to note that the sense of this spin with this particular model geometry tends to *increase* the Schmid factor of the band by rotating the lattice within it away from the tensile axis (i.e. toward a 45 degree orientation which maximizes the Schmid factor for this idealized geometry) *relative* to the lattice in the surrounding parts of the crystal. Thus the kinematics of localized shearing imply a "local geometrical softening" of the slip plane with which the shear band is nearly aligned. Rotations of this type have been experimentally documented as described below.

4. Experimental results

A series of tension and compression tests were carried out at room temperature on single crystals of Al-3 wt percent Cu aged to contain GPI and GPII zones, and θ' precipitates. Most crystals were initially aligned for single slip on the (111) $[\bar{1}01]$ (primary) slip system. A full report of the mechanics of band formation will be the subject of a forthcoming report. Here we briefly note that there were important qualitative differences in the way bands developed in the various microstructures. Crystals with θ' precipitates developed shear bands, in tension, only after load maximum and small amounts of necking as suggested by the model, and usually before the tensile axis reached the [001]–$[\bar{1}11]$ symmetry boundary. These bands were nearly aligned with the primary slip system. For the underaged microstructures containing GPI or GPII zones, however, the shear bands were proceeded by the formation of "coarse slip bands" which were nearly aligned with either the primary or conjugate system and, in tension, which occasionally appeared while

the load-extension curve was still rising. Furthermore, for all the microstructures localized flow was often observed to progress alternately on the primary and conjugate systems leading to a double wedge [6] fracture mode. Finally, we note that in *all* cases macroscopic localized shearing began while the crystals were strain-hardening — there was no evidence of either softening or fracture (i.e. void or microcrack initiation) preceding shear band formation. For crystals covering a rather wide range of initial orientations, and for *all* microstructures, the critical ratio (h/σ) where *macroscopic* localized shearing set in was found to be sensibly constant with an average value equal to $(h/\sigma)_{\text{critical}} \approx 0.035$. This compares favorably with the range $0.40 < (h/\sigma)_{\text{critical}} < 0.064$ predicted by our simple model. The "coarse slip bands" that formed in the zone-hardened crystals, and in which macroscopic localized shearing set in, may be viewed as material imperfections that strain-harden at a lower rate than the surrounding crystal.

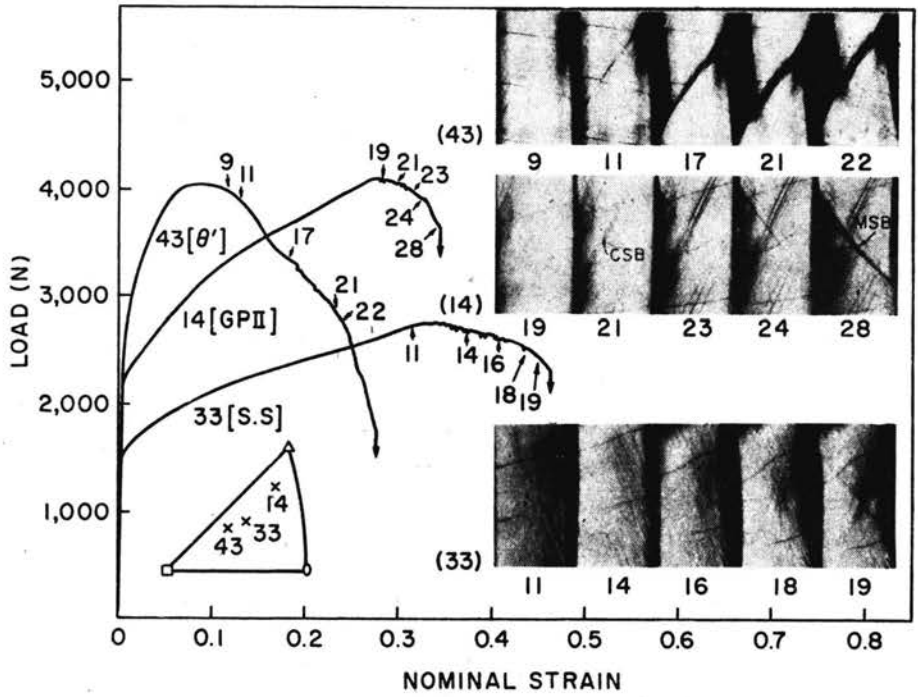

FIG. 4. Typical load-nominal strain curves for the three microstructures containing GPI, and GPII zones and θ' precipitates along with in-situ micrographs taken at the indicated stages of deformation. Note the load drop, apparently accompanying localized shearing, in the GPI microstructure and that macroscopic localized shearing only occurs after the load maximum (and the onset of necking) in all the microstructures.

Figure 4 shows typical load-extension curves together with corresponding surface micrographs taken in-situ at the indicated stages of deformation. As implied by our choice of examples, underaged crystals initially oriented for double slip displayed the largest load drops accompanying shear band formation, often as large as 130 N. Loads drops were commonly, but not always, observed in all three microstructures.

Micrographs of shear bands formed in tension and compression are shown in Figs. 5a

and 5b, respectively. One of the particular noteworthy features of the band in Fig. 5a, common to all shear bands, is the difference in orientation between its *material* plane and the slip planes of the surrounding lattice. The trace of the primary slip plane is marked, approximately and as confirmed by x-ray diffraction, by the slip traces labelled S. The

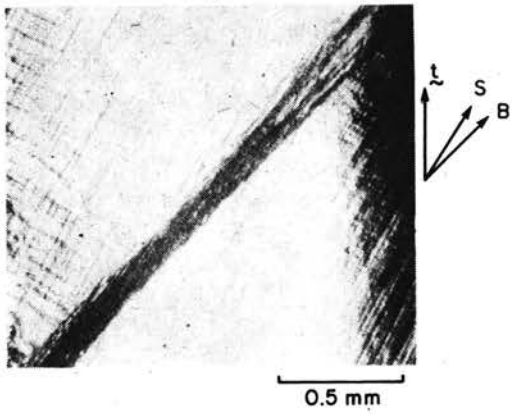

a

b

FIG. 5. Macroscopic shear bands in tension and compression specimens. Note in (a) how the slip traces intersect the shear band indicating a difference in orientation between the operative slip planes and the shear band. A full description is given in the text.

angle between S and the tensile axis, $\mathbf{t}$, is about 30 degrees whereas between the material plane of the band, B, and $\mathbf{t}$ it is about 40 degrees. As described in the next section, x-ray evidence shows that the lattice in the *band* is also rotated with respect to that of the surrounding crystal in the same way — in other words so that the traces of the primary slip plane in the band rotate from S toward B. Such rotation would lead to an increase in the Schmid factor, as described in Fig. 9, in the band thereby encouraging increased deformation on its primary planes.

4.1. Lattice rotation

A general feature of single crystal plasticity is that the load axis rotates along a great circle toward the $[\bar{1}01]$ or [111] pole with tensile or compressive straining in fcc crystals undergoing essentially single slip [10]. Our x-ray studies confirmed that this was indeed the case. To study non-uniform lattice rotations occurring within shear bands as indicated

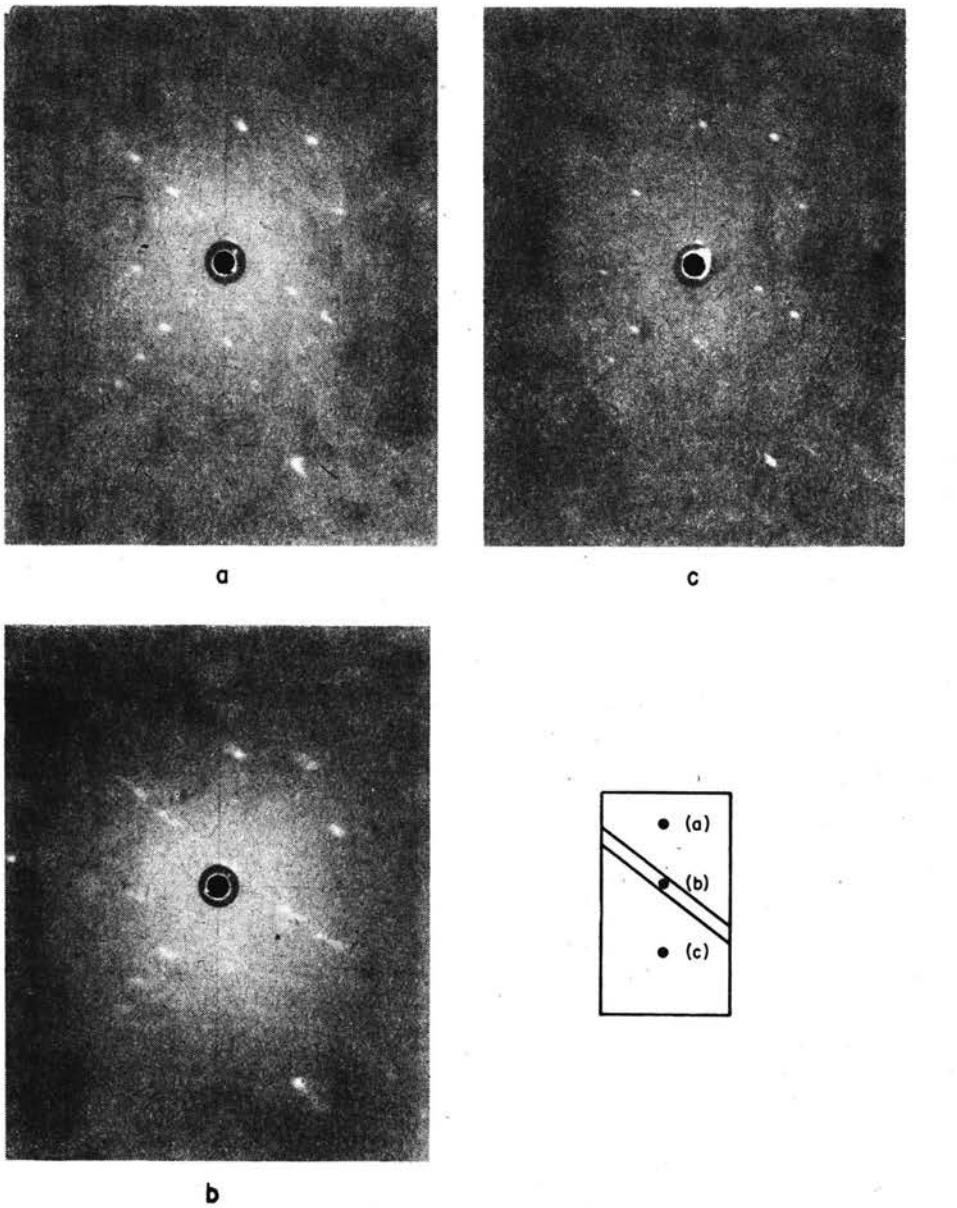

FIG. 6. Laue back reflection diffraction patterns taken at points on the crystal's surface, relative to a macroscopic shear band as indicated. One-half mm collimator was used.

by Eq. (3.12), Laue back reflection diffraction patterns were taken from the shear band and surrounding regions and analyzed stereographically. Figure 6 shows results that are typical for all three microstructures. We note though, that crystals with a θ' microstructure were more difficult to analyze due to additional complex patterns of lattice rotation caused by necking.

As shown by Fig. 6, diffraction patterns taken from the shear band regions displayed severe asterisms characterized by unidirectional streaking with double intensity maxima, whereas patterns taken outside the bands had no noticeable asterism. Furthermore, it was found that the lattice on either side of the band had the same orientation and, as indicated in Fig. 7, that one of the intensity peaks in the shear band pattern precisely

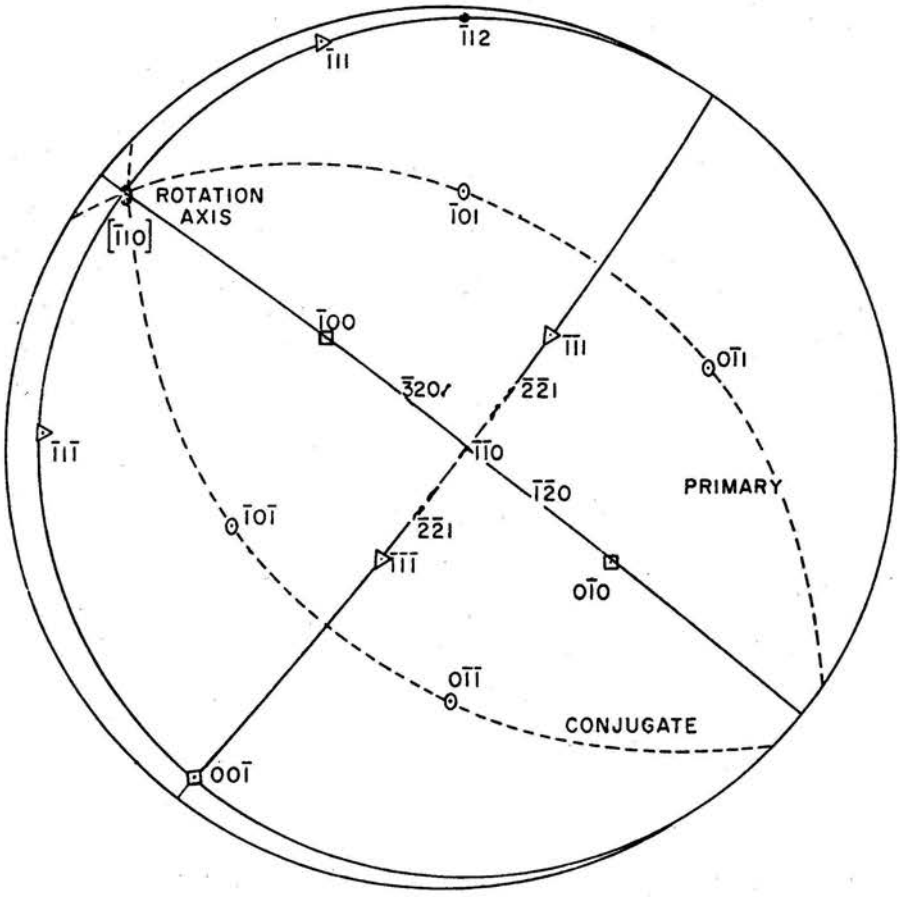

FIG. 7. Analysis of the diffraction patterns shown in Figure 6. The streaks correspond to a lattice misorientation of the band with respect to the surrounding matrix produced by a rotation of approximately 4 degrees about the $[\bar{1}10]$ axis.

coincided with that of the matrix. For the particular example shown in Figs. 6 and 7, the remaining peak in the band was rotated counterclockwise approximately 4 degrees about the $[1\bar{1}0]$ axis — this is the direction of intersection of the primary and conjugate

slip planes. This axis and direction of rotation were identical for all crystals; the amount of rotation varied but generally appeared to increase with strain accumulation in the bands.

The x-ray diffraction results were qualitatively supported by Berg-Barrett x-ray microscopy [11] of the shear bands. Figure 8 is an example in which the orientation contrast [12]

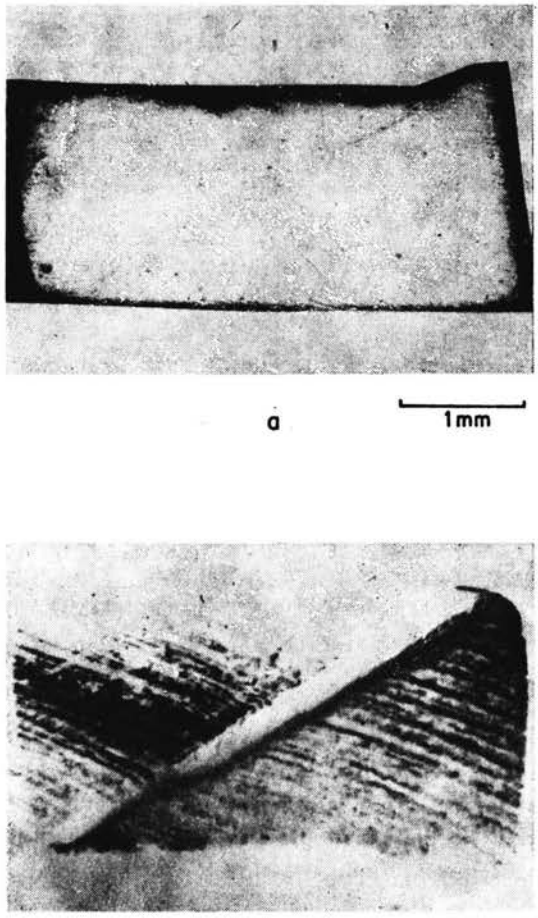

FIG. 8. Optical micrograph of a sectioned, electro-polished and etched crystal containing a macroscopic shear band. A Berg-Barrett topograph of [$\bar{1}$12] surface using [$\bar{1}$11] reflection is shown in (b). Note the abrupt change in orientation contrast indicating rather discontinuous change in orientation across the band's surface.

of the band versus the surrounding crystal further demonstrates that the lattice misorientation can be quite abrupt and even appear discontinuous across the band.

It is, of course, important to note that in all cases, in tension and compression, the observed rotations increased the Schmid factor in the bands relative to the matrix — the bands become "geometrically soft".

Figure 9 illustrates this further by displaying the poles of the tensile axis in the bands and surrounding crystal for four specimens. The initial orientation is denoted by x; the

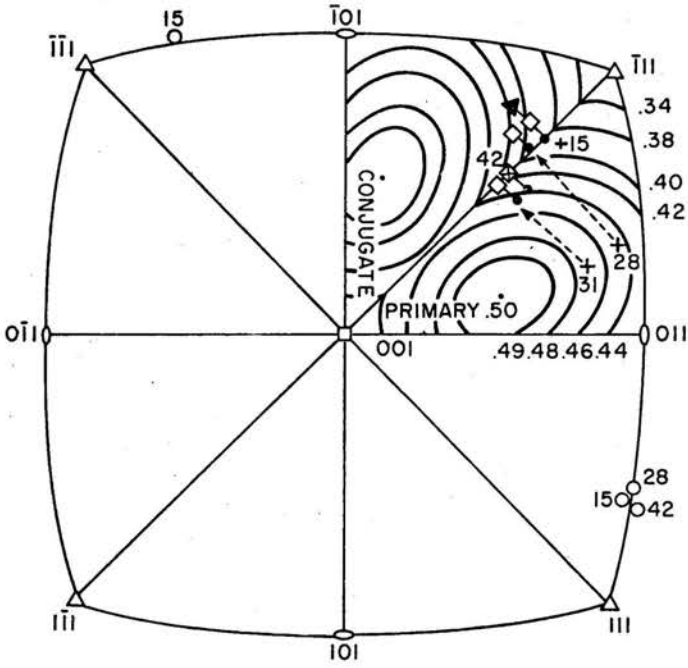

FIG. 9. Stereographic representation of the poles of tensile axes, before and after deformation, in various shear bands and in the surrounding matrix. As explained in the text, the poles of the bands (marked by closed dots) indicate, when compared with respect to orientation with those of the matrix (marked by open squares), that the bands are "geometrically soft". Open circles represent the poles of macroscopic shear bands.

orientations after deformation for the tensile axis in the band is marked by a closed dot and in the surrounding crystal (or matrix) by an open square. For the crystals labelled 28, 31 and 42 the bands were nearly parallel to the primary plane — thus the positions of the bands' poles indicate a higher Schmid factor in the band than in the matrix. A few contours of the Schmid factor are indicated in the figure for the reader's convenience — more detailed information is widely available [10]. Crystal 15 is particularly interesting in that there were two bands formed, nearly parallel to the primary and conjugate slip planes. The pole of the tensile axis in the "conjugate band" is marked by the closed triangle. Here again it may be seen that the Schmid factors are higher on the slip system to which the corresponding shear bands is nearly parallel — in this sense both bands become geometrically soft and encourage larger strains to develop.

The stereogram of Fig. 9 also shows the poles of the material planes of the shear band — the rotation from the (111) poles of the primary slip plane is evident.

Crystals tested in compression also showed severe streaking without any intensity maxima in diffraction patterns. But it was even more difficult to analyze the patterns precisely because of the complex asterism induced by small amounts of buckling that often occurred very soon after localized shearing. However, we were able to determine that the streaks of the shear bands also corresponded to a $[0\bar{1}1]$ rotation axis.

5. Dislocation interactions

We seek here a possible description for the observed local lattice rotation in terms of dislocation interactions. We begin with the case of tension.

As the tensile axis undergoes a general rotation toward the $[\bar{1}01]$ pole, the conjugate

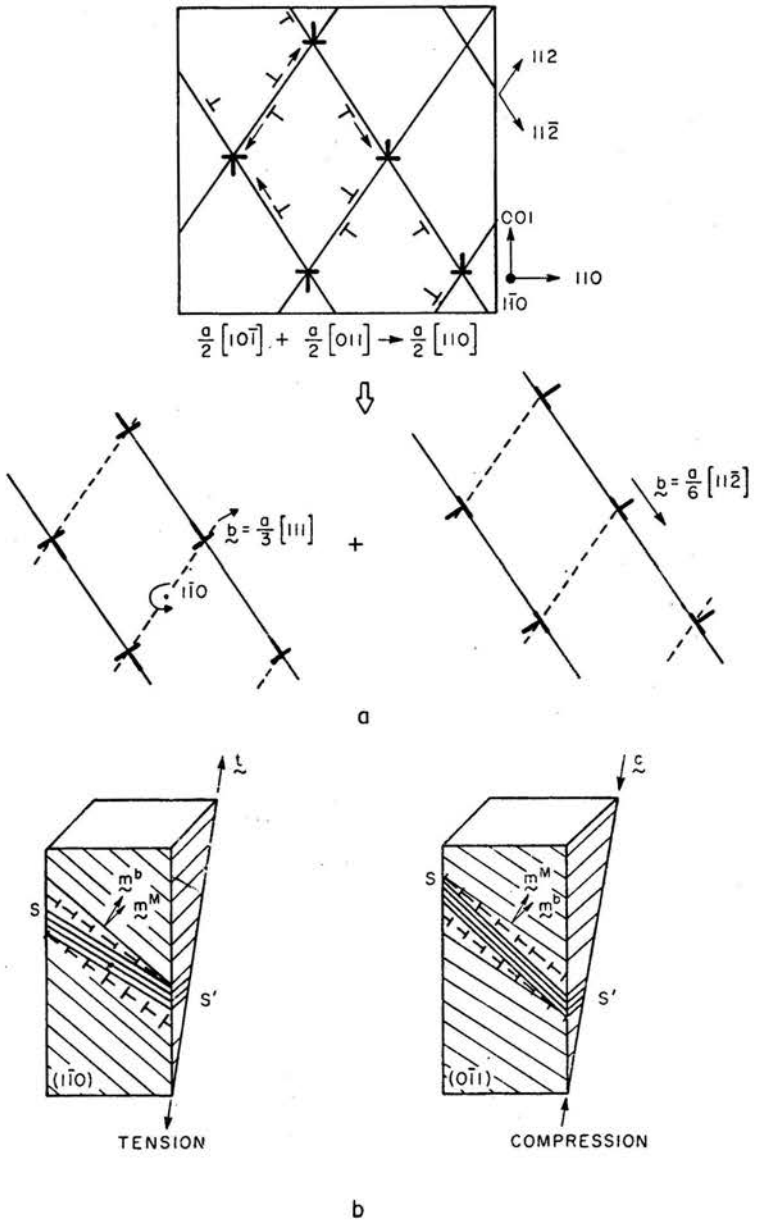

FIG. 10. Dislocation arrays, formed by interaction of primary and conjugate dislocations, that give rise to the "local lattice rotations" shown in Fig. 6.

slip system becomes highly stressed. When the tensile axis approaches the [001]–[$\bar{1}$11] boundary, interactions between primary and conjugate dislocations become frequent and lead, as is well known, to the formation of Lomer-Cottrell (L-C) dislocations [13] — the reaction can be written as

$$\frac{a}{2}[10\bar{1}]+\frac{a}{2}[011]\rightarrow\frac{a}{2}[110]\ldots\text{along }[1\bar{1}0]. \tag{5.1}$$

The Burgers vectors of the L-C dislocations can be conveniently thought of as consisting of two edge components,

$$\frac{a}{2}[110]\rightarrow\frac{a}{6}[11\bar{2}]+\frac{a}{3}[111] \tag{5.2}_1$$

or

$$\frac{a}{2}[110]\rightarrow\frac{a}{6}[112]+\frac{a}{3}[11\bar{1}] \tag{5.2}_2$$

when they form on the primary or conjugate slip planes, respectively. This is schematically illustrated, following WILKENS' discussion [14] in Fig. 10. The edge components $\frac{a}{6}[11\bar{2}]$ or $\frac{a}{6}[112]$ form a Taylor lattice and do not cause any rotation whereas the edge dislocations $\frac{a}{3}[111]$ and $\frac{a}{3}[11\bar{1}]$, when arrayed on the primary or conjugate planes, form sub-boundaries and thus cause local lattice rotation. The rotation axis is the intersection between the primary and conjugate slip planes, [1$\bar{1}$0], and the sense of rotation always tends to *increase* the Schmid factor between the layers of L-C dislocations. Both these results are in accord with our experimental findings.

Similary we anticipate L-C dislocation formation in compression as the load axis approaches the [001]–[011] boundary. On this boundary the load axis tends to rotate toward the [011] pole. Thus four slip systems, viz., $(111)\frac{a}{2}[\bar{1}01]$, $(111)\frac{a}{2}[\bar{1}10]$, $(\bar{1}11)\frac{a}{2}[101]$, and $(\bar{1}11)\frac{a}{2}[110]$ become highly stressed. The pairs $(111)\frac{a}{2}[\bar{1}01]$, $(\bar{1}11)\frac{a}{2}[110]$ and $(\bar{1}11)\frac{a}{2}[101]$, $(111)\frac{a}{2}[\bar{1}10]$ can form L-C dislocations,

$$\frac{a}{2}[\bar{1}01]+\frac{a}{2}[110]\rightarrow\frac{a}{2}[011]\ldots\text{on the primary plane} \tag{5.3}_1$$

and

$$\frac{a}{2}[\bar{1}10]+\frac{a}{2}[101]\rightarrow\frac{a}{2}[011]\ldots\text{on the critical plane} \tag{5.3}_2$$

The Burgers vector of the L-C dislocations can also be thought of as consisting of two edge components, viz.,

$$\frac{a}{2}[011] \rightarrow \frac{a}{3}[111] + \frac{a}{6}[\bar{2}11]$$

(5.4) or

$$\frac{a}{2}[011] \rightarrow \frac{a}{3}[\bar{1}11] + \frac{a}{6}[211]$$

depending upon the active slip system. The rotation axis, in both cases, is found to be $[0\bar{1}1]$ and again, the crystal lattice will be rotated locally so as to increase the Schmid factor in the region between the two layers of L-C dislocation boundaries.

Figure 10b provides a schematic view of the lattice rotations in tension and compression.

6. Discussion

Although shear bands were always nearly aligned with one of the active slip systems, surface studies consistently showed that their material planes were rotated finite amounts with respect to the slip plane in the adjacent parts of the crystal. For a well-developed band these rotations were as much as 10 degrees and always with a sense that lines such as SS' in Fig. 10b, which originally were meant to be traces of the active slip planes in the bands, *could* — that is, in terms of the sense of rotation also represent the material plane of the band. Precise correlations are not possible due to uncertainties in the absolute length of streaks in the Laue patterns, but available evidence suggests that the macroscopic planes of the bands were usually *further* misaligned with the slip planes outside than were the band's slip planes. Lattice misorientations across shear bands rarely exceeded about 4 degrees. The orientation of the shear bands we note is in qualitative agreement with the model predictions highlighted in Fig. 3.

As described by PRICE and KELLY [3], shear bands are often accompanied by load drops — the magnitudes of which we found to be dependent on microstructure and with the expected degree of local geometrical softening. For example, when the tensile axis is near the [001]–[111] boundary, a rotation of 3–4 degrees typically raises the Schmid factor in the band by about 0.01 above that in the matrix. This, using typical values for the flow stress and dimensions of these crystals, corresponds to a 90N load increment which, as previously noted, was typical in the tests on underaged crystals.

The experiments just described suggest that the description of localized shearing in ductile single crystals put forth here is essentially correct. Our crystallographic studies of localized shearing have shown that shear bands in Al—Cu crystals at least are characterized by finite lattice rotations. These rotations have the important mechanical significate of rendering the bands geometrically softer than the surrounding crystal. The existence and nature of these rotations are natural consequences of the kinematics of localized shearing and, as described above, are in essential agreement with the predictions of our model boundary value problem for crystalline deformation. This work suggests that the kinematics of localized shearing in single crystals be studied experimentally for other

materials, including pure, single phase metals, and that an analysis of the mechanics of shear band formation, of the type introduced by Asaro for a model crystal geometry, be carried out using the actual crystallography for fcc and bcc crystals. The theoretical procedures for doing this have been described in Sects. 2 and 3.

Acknowledgements

We are pleased to acknowledge the helpful discussions we have had with Professors J. R. RICE and A. NEEDLEMAN. This work was supported by the Materials Science Division of the National Science Foundation under Grant DMR 76-20642. The experimental position of our research was made possible through the use of equipment in the Central Facility of the Brown Materials Research Laboratory.

References

1. R. J. ASARO, Acta Metall., **27**, 445, 1979.
2. R. J. ASARO and J. R. RICE, J. Mech. Phys. Solids, **25**, 309, 1977.
3. R. J. PRICE and A. KELLY, Acta Metall., **12**, 974, 1964.
4. E. HORNBOGEN and K. GAHR, Metallography, **8**, 181, 1975.
5. R. HILL and J. W. HUTCHINSON, J. Mech. Phys. Solids., **23**, 239, 1975.
6. J. MILES, Arch. Mech. [to be published 1981].
7. R. HILL and J. R. RICE, J. Mech. Phys. Solids, **20**, 401, 1972.
8. M. A. BIOT, *Mechanics of incremental deformation*, Wiley, New York 1965.
9. C. N. REID, A. GILBERT, and G. T. HAHN, Acta Metall., **14**, 975, 1966.
10. C. N. REID, *Deformation geometry for materials scientists*, Pergamon Press, Oxford 1973.
11. B. ROESSLER and R. W. ARMSTRONG, Advan. X-ray Analysis, **12**, 139, 1969.
12. M. WILKENS, Can. J. Phys., **45**, 567, 1967.
13. F. R. N. NABARRO, Z. S. BASINSKI and D. B. HOLT, Advan. Phys., **13**, 193, 1964.
14. B. OBST, H. AVER and M. WILKENS, Mat. Sci. Eng., **3**, 41, 1968–69.

BROWN UNIVERSITY
DIVISION OF ENGINEERING, PROVIDENCE, RHODE ISLAND, USA.

Received September 26, 1979.